ACS Photonics

Article

Cite This: ACS Photonics 2019, 6, 2133−2140

pubs.acs.org/journal/apchd5

Photothermal Modulation of Propagating Surface Plasmons on Silver Nanowires

Qiang Li,[†,‡,∥] Li Chen,[§,∥] Hongxing Xu,[⊥] Zhaowei Liu,[§,#] and Hong Wei*[,†,▽]

[†]Institute of Physics, Chinese Academy of Sciences, Beijing 100190, China

[‡]Guangdong Provincial Key Laboratory of Nanophotonic Functional Materials and Devices, School of Information and Optoelectronic Science and Engineering, South China Normal University, Guangzhou 510006, China

[§]Materials Science and Engineering, University of California, San Diego, 9500 Gilman Drive, La Jolla, California 92093, United States

[⊥]School of Physics and Technology, and Institute for Advanced Studies, Wuhan University, Wuhan 430072, China

[#]Department of Electrical and Computer Engineering, University of California, San Diego, 9500 Gilman Drive, La Jolla, California 92093, United States

[▽]Songshan Lake Materials Laboratory, Dongguan, Guangdong 523808, China

Supporting Information

ABSTRACT: Nanoplasmonic devices have received much attention in recent years due to their ability to confine light beyond the diffraction limit. Manipulating the propagation of surface plasmons (SPs) is of vital importance for the creation of nanometer-scale integrated photonic devices. In this work we exploit the photothermal property of a silver nanowire (NW) to optically modulate the propagation of SPs on it. Under the excitation of a control laser beam, the rise of local temperature induced by the photothermal effect of silver NW results in the dramatic increase or decrease of the intensity of the transmitted SPs generated by a probe laser beam, depending on the Fabry-Pérot resonance conditions of the SPs on the NW. The amplitude of the photothermal modulation depth is found to be strongly dependent on the focal position, polarization, and power of the control beam. The simulations reveal that the high modulation depth at the NW end is mainly caused by the additional heat generated by the propagating SPs on the NW. The analytical solutions for the transmissivity and modulation depth are presented. Both numerical simulations and theoretical analysis agree well with the experimental results. Our work provides not only a new kind of all-optical modulation method for the propagating SPs in ultracompact plasmonic devices, but also the basic understanding about the influence of environmental temperature on the propagating SPs.

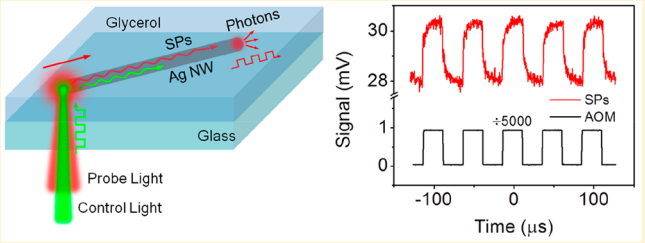

KEYWORDS: *photothermal modulation, thermo-optic effect, propagating surface plasmons, nanowires, plasmonic waveguides, Fabry-Pérot resonators*

Surface plasmons (SPs), the electromagnetic excitation of electron oscillations propagating on the metal−dielectric interface with subwavelength field confinement, are becoming widely accepted as a prospective type of optical information carrier in ultracompact integrated photonic circuits.[1,2] Optical signals in the form of SPs can be efficiently guided and manipulated in plasmonic waveguides. A number of experiments have demonstrated the transmission of SPs in various types of waveguides, such as metal nanowires (NWs),[3−6] metal stripes,[7] and grooves and slots in metal film.[8,9] Chemically synthesized Ag NWs with the size of cross section well below the diffraction limit are highly compact and high-quality waveguides for long distance propagation of SPs.[10] Propagating SPs on Ag NW are partly reflected back and forth between the two NW terminals and the Ag NW can be regarded as a Fabry-Pérot (FP) resonator.[11] Many fundamental properties of the propagating SPs on Ag NW waveguides have been revealed, such as the superposition of different SP modes,[12−14] the direction and polarization of the scattered SPs at the terminal of the NW,[15,16] and the plasmon−exciton interaction with the coupled quantum emitters.[17−19] Optical signal processing functionalities, including routing[20−22] and logic functions,[23,24] have been proposed and demonstrated in Ag NW networks.

The active control of propagating SPs is a crucial step toward the realization of highly integrated optical communication and computing networks. The main characteristics of the propagating SPs, including wave vector and propagation length, are very sensitive to the permittivity of the metal waveguide and the surrounding dielectric environment.[25] Thus, the main promising routes toward the realization of signal switching and modulation on plasmonic waveguides

Received: May 17, 2019
Published: June 25, 2019

DOI: 10.1021/acsphotonics.9b00711
ACS Photonics 2019, 6, 2133−2140

involve the use of appropriate materials whose permittivity can be controlled actively and reversibly. In the past few years, the active plasmonic modulators and switches have been successfully realized through the use of thermo-optic (TO),[26−28] electro-optic,[29−31] and nonlinear optical effects,[32,33] phase change[34] and photochromic materials,[35,36] gain materials,[37] and so on.

The use of TO dielectric material whose refractive index is dependent on temperature is one of the most practical ways to realize the active control of propagating SPs on a waveguide. Thermally induced small changes of permittivity can modify the wave vector and the propagation length of SPs, and significantly alter the electromagnetic field distribution within waveguides and the transmission of SPs. In a typical TO modulator and switch, the thermal energy is usually from the Joule effect of the electric current flowing inside the metallic parts of plasmonic waveguides.[26,28] The electrically driven heat generation requires careful design of the conductive route, which is an extra load of the plasmonic waveguide and puts a limitation on the integration of plasmonic devices. Photothermal effect is an alternative approach for the activation of TO modulation and switching.[27,38−41] Plasmonic nanostructures themselves can be used as efficient and flexible heat sources under light illumination and have shown exciting potential applications in the fields such as photothermal cancer therapy[42,43] and drug delivery,[44,45] as well as optical imaging and spectroscopy.[46−49] The photothermally activated modulators and switches can be implemented to minimize the size and improve the integration level of plasmonic circuits.

Here in this paper, we systematically studied the influence of photothermal effect on the propagation of SPs on Ag NWs surrounded by glycerol. Because of the TO properties of silver and glycerol, the local temperature rises under the excitation of a control laser beam of 532 nm wavelength, resulting in the reduction of wave vector and propagation length of propagating SPs. As the Ag NW can be regarded as a FP cavity, the intensity of the transmitted SPs generated by a probe laser beam of 785 nm wavelength is increased or decreased dramatically upon the control beam illumination, depending on the FP resonance conditions of SPs on the NW. The amplitude of the photothermal modulation depth is strongly dependent on the focal position, polarization, and power of the control beam, which is caused by the difference of heat generated under different excitation conditions. The heat generation induced by the propagating SPs is analyzed and discussed in detail, which contributes to the polarization-dependent higher modulation depth at the NW ends. The analytical solutions for the transmissivity and the modulation depth are provided, which agree well with the experimental results and provide the basic understanding about the photothermal response of the propagating SPs. We also studied the dynamic photothermal response of the propagating SPs on Ag NW, which provides a response time of about 5 μs.

RESULTS AND DISCUSSION

The sample consisted of chemically synthesized Ag NWs with diameter of about 120 nm placed on top of the glass substrate and immersed in glycerol with high TO coefficient and low thermal conductivity. The experimental setup is schematically shown in Figure 1. After passing through the acousto-optic modulator (AOM), the control laser beam of 532 nm wavelength was expanded by a spatial filter system. Its focal position on the sample plane was steered using a galvanometer scanning mirror system with a step size of 40 nm. The probe laser beam of 785 nm wavelength was focused on one end of the NW to excite the propagating SPs. The scattered SPs at the other end of the NW passed through an interference filter to block the control laser light and were then directed to an avalanche photodiode through a spatial filter system. The intensity of the transmitted SPs P in the absence of control laser beam was recorded by a digital voltmeter. The intensity variations of the transmitted SPs δP induced by the control laser beam was obtained by using a lock-in amplifier referring to the frequency of the AOM. The modulation depth is defined as $\delta P/P$.

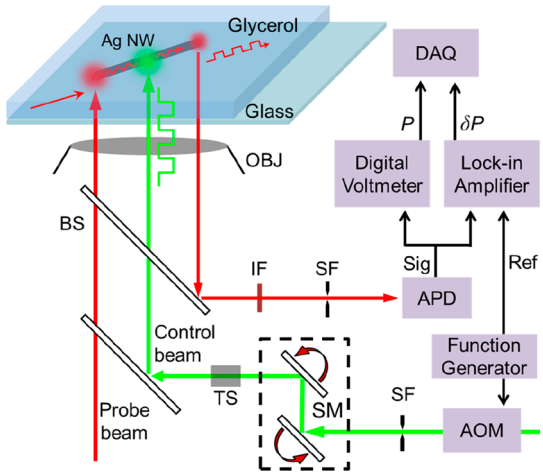

Figure 1. Scheme of experimental system for photothermal modulation of propagating SPs on Ag NW. A probe laser beam of 785 nm wavelength was used to generate propagating SPs, which were all-optically modulated by a control laser beam of 532 nm wavelength through the photothermal effect. OBJ, AOM, SM, BS, IF, SF, TS, APD, and DAQ represent oil objective, acousto-optic modulator, galvanometer scanning mirror, beam splitter, interference filter, spatial filter, telescope, avalanche photodiode, and data acquisition, respectively. Sig and Ref refer to the voltage signal from the APD and function generator, respectively. The half-wave plates and camera are not shown in the scheme.

We found that the measured modulation depth can be either positive or negative for different NWs, that is, the control beam can result in the intensity enhancement or attenuation of the transmitted SPs at the NW end. Figure 2a−e show the typical result of a Ag NW (NW I) whose modulation depth is positive. The scanning electron microscope (SEM) image of the NW (Figure 2a) reveals a NW diameter of 123 nm. Figure 2b shows the scattering image when the probe laser beam was focused onto the NW end A. The polarization of the probe laser beam is parallel to the NW axis. The bright spot at end B of the NW indicates that propagating SPs have been launched and coupled out as photons. Figure 2c shows the distribution of the obtained modulation depth when the focal spot of the control laser beam scanned across the whole NW with a step size of 40 nm. The power of the control beam is 1.3 mW. The polarization of the control laser beam is parallel to the NW axis. As can be seen, the distribution of the modulation depth is uniform along the NW except the NW ends where the modulation depth is about 5.2× as high as that along the NW surface. The distribution of the modulation depth for the control beam polarized perpendicular to the NW axis (Figure 2d) is similar to that of Figure 2c, but with a higher modulation depth on the NW surface and a lower signal at the two NW

DOI: 10.1021/acsphotonics.9b00711
ACS Photonics 2019, 6, 2133−2140

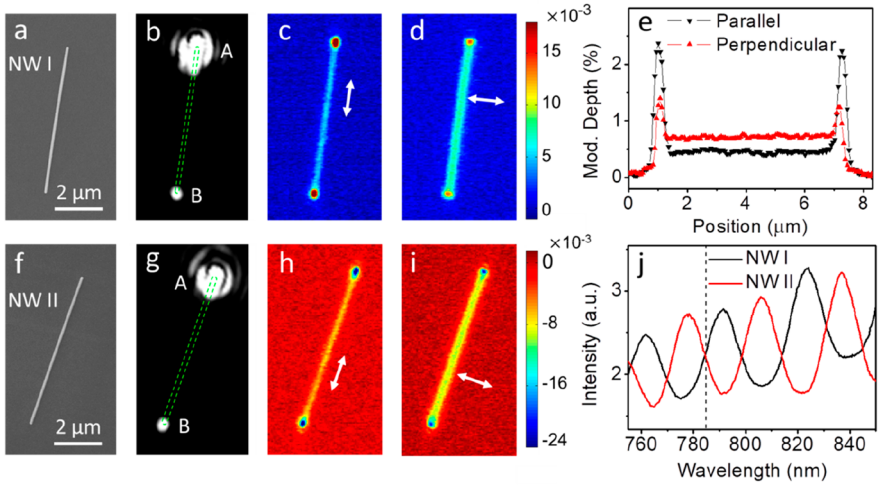

Figure 2. (a) SEM image of a typical Ag NW whose modulation depth is positive. The measured NW diameter and length are 123 and 6195 nm, respectively. (b) Optical scattering image of the investigated NW when the probe laser beam of 785 nm wavelength was focused on the NW end A. The dash lines mark the outline of the NW. (c, d) Measured modulation depth of the transmitted SPs at the NW end B as a function of the focal position of the control beam. Here the signal along the NW is positive, which means the photothermal effect enhances the intensity of the transmitted SPs. The polarization of the control beam is parallel (c) and perpendicular (d) to the NW axis, as indicated by the white arrows. (e) Distributions of modulation depth along the NW when the polarization of control beam is parallel (black dot line) and perpendicular (red dot line) to the NW axis. (f–i) The same as (a)–(d), but for another Ag NW whose modulation depth is negative. The measured NW diameter and length are 119 and 6486 nm, respectively. (j) Measured transmission spectra of the two NWs shown in (a)–(d) and (f)–(i). The dash line marks the wavelength of 785 nm. The power and modulation frequency of the control beam was 1.3 mW and 80 kHz, respectively.

ends (Figure 2e). Figure 2f–i show the SEM image, the scattering image, and the distributions of the modulation depth of another NW (NW II) whose modulation depth is negative. The dependence of modulation depth on the focal position and polarization of the control beam is the same as that of Figure 2c,d. We measured the transmission spectra of the two NWs without the control beam illumination (Figure 2j) by focusing the white light from a supercontinuum laser source onto the end A of the NW to excite the propagating SPs and detecting the spectrum of the scattered light from the end B of the NW. The transmission spectra show distinct line shapes of FP resonance modes which are caused by the interference of propagating SPs partly reflected back and forth between the two NW terminals. It is found that the 785 nm wavelength of the probe light is on the rising slope and falling slope of the spectra for NW I and NW II, respectively. For a given NW, the positive and negative modulation depth can be obtained by tuning the wavelength of the probe beam.

To better understand the dependence of the modulation depth of propagating SPs on the focal position and polarization of the control beam, we performed simulations of the photothermal modulation process by using a finite-element method based commercial software COMSOL Multiphysics. The system is modeled as a cylindrical Ag NW lying on a glass substrate with glycerol on top as shown in Figure 1. The diameter and length of the NW are 120 nm and 6.29 μm, respectively. The control beam was set as a Gaussian beam with beam waist of 0.8 μm and wavelength of 532 nm. The initial environment temperature was set as room temperature of 23 °C. The thermal and optical parameters of silver, glass, and glycerol used in simulation are provided in Section 1 of Supporting Information. With the "Wave Optics-Frequency Domain" module and "Heat Transfer" module in COMSOL Multiphysics, a three-step simulation was performed to gradually calculate the ohmic loss generated by the control beam, the heating process due to ohmic loss, and the final transmission of SPs excited by the probe beam after the rise of temperature. The black line in Figure 3a shows the simulated transmission spectrum without the control beam. Similar to the experimental result (Figure 2j), the transmission spectrum represents the line shape of FP resonance behavior. The Ag NW is an efficient localized heat source upon the illumination of control beam. The rise of local temperature leads to the changes of permittivity of both glycerol and Ag NW, which, in turn, influence the wave vector and the propagation length of the SPs on the Ag NW. The red, blue, and pink lines in Figure 3a represent the transmission spectra when the control beam polarized perpendicular to the NW with power of 10, 20, and 50 mW was focused on the middle section of the NW, respectively. With the increase of the control beam power, the transmission spectra show clear blue shift, which results in the increase or decrease of the transmitted SP intensity, depending on the wavelength. The simulation results for different environment temperature show that the wave vector and propagation length of the SPs on the Ag NW are both decreased with the increase of the temperature (see Section 2 of Supporting Information). For the probe beam of 785 nm wavelength, we scanned the spot of control beam (10 mW) along the NW with a step size of 100 nm and obtained the distributions of the modulation depth. As shown in Figure 3b, the simulation results show similar distributions to the experimentally measured photothermal modulation depth along the NW (Figure 2e). Since the 785 nm wavelength is in the monotonically rising slope of the transmission spectrum, the sign of the modulation depth is positive due to the blue shift of transmission spectrum.

Figure 3c,e present the electric field distributions around the NW when the control beam is focused at the middle section of the NW. When the control beam is polarized parallel to the NW axis, the Ag NW can be regarded as a shading obstacle and the incident control beam is simply diffracted. The enlarged view of the near-field distribution at the control beam position

DOI: 10.1021/acsphotonics.9b00711
ACS Photonics 2019, 6, 2133–2140

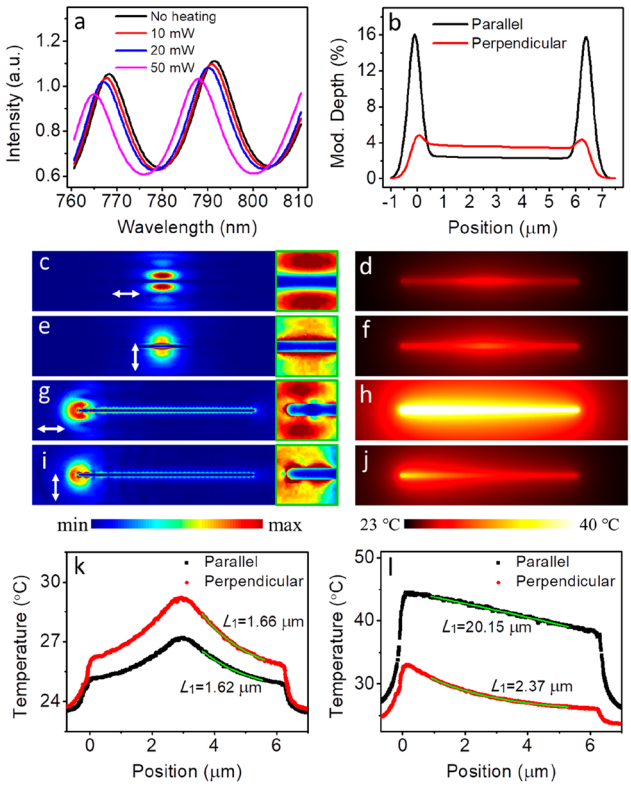

Figure 3. (a) Transmission spectra without (black line) and with the control beam of 10 (red line), 20 (blue line), and 50 mW (pink line) focused on the middle section of the Ag NW. (b) Distributions of modulation depth along the NW axis for the control beam polarized parallel (black line) and perpendicular (red line) to the NW. The wavelength of the probe beam is 785 nm. (c–j) Distributions of electric field amplitude (c, e, g, i) and the corresponding temperature (d, f, h, j) at the plane 60 nm above the surface of glass substrate when the control beam was focused at the middle (c–f) and the end (g–j) of the NW with the polarization parallel (c, d, g, h) and perpendicular (e, f, i, j) to the NW. The polarization of the control beam is indicated by the white arrows. The enlarged views of the electric field distributions at the control beam position are shown in the green line boxes. The power of the control beam is 10 mW for (b–j). (k, l) Temperature distributions along the NW axis in (d, f) and (h, j), respectively. The green solid lines represent the fitting of the data for the selected sections using the equation "$T = A_1\exp(-z/L_1) + T_0$". The fitted results of L_1 are written in the figure.

shows that the electric field is mainly concentrated in the medium of glycerol (Figure 3c). For the case of perpendicular polarization, the localized SPs are excited and the electric field is strongly concentrated around the NW surface (Figure 3e). After integrating the electric field induced ohmic loss on the Ag NW, we found that the thermal power is 18.4 and 27.2 μW for the incident polarization parallel and perpendicular to the NW axis, respectively. The section of the NW under control beam illumination can be simply treated as a point heat source. The heat energy is conducted along the NW and dissipated into the glycerol. Figure 3d,f show the corresponding temperature distributions around the NW. The temperature along the NW decreases away from the heating area (Figure 3k). A single exponential decay fitting provides the temperature decay length of about 1.6 μm, which is determined by the geometry and thermal parameters of silver, glass, and glycerol. The higher thermal power for control beam polarized perpendicular to the NW axis results in higher temperature increase and larger modulation depth (Figure 3b).

Figure 3g–j show the electric field and the corresponding temperature distributions around the NW when the control beam is focused at the end of the NW. Clearly, propagating SPs are generated and propagate along the NW (see Section 3 of Supporting Information). Here the thermal power on the NW can be separated into two parts. One is from the ohmic loss generated at the position of the incident control beam and the other part is from the ohmic loss induced by the propagating SPs on the NW. The two parts can be treated as point heat source at the NW end and line heat source along the NW, respectively. The thermal power of these two parts is 30.3 and 75.9 μW for the polarization parallel to the NW axis and 21.8 and 13.4 μW for the polarization perpendicular to the NW axis, respectively. Therefore, the total thermal power generated by focusing the control beam on the NW end is 106.2 and 35.2 μW for parallel and perpendicular polarization, respectively. The higher thermal power for the parallel polarization is caused by the higher excitation efficiency of propagating SPs, which results in higher temperature around the NW (Figure 3h,j). The corresponding temperature distributions along the NW under the excitation with the two different polarizations (Figure 3l) result in the temperature decay length of 20.15 and 2.37 μm, respectively. The increased temperature decay length compared with the NW upon middle excitation is caused by the existence of line heat source along the NW generated by the propagation of SPs on the NW. The longer temperature decay length for the parallel polarization is caused by the higher ratio of the thermal power between the line heat source and the point heat source. By comparing the thermal power of the NW upon middle excitation and end excitation, we found that the thermal power generated by the propagating SPs on the NW is the main reason for the larger modulation depth at the NW ends (Figure 3b). As far as we know, it is the first time that the heat generation induced by propagating SPs is analyzed, which is important for the design of highly efficient photothermal heat sources and provides an efficient way to increase the photothermal modulation depth.

In order to find the relationship between the sign of photothermal modulation depth and the slope value of the transmission spectra, we theoretically analyzed the influence of temperature rise on the wave vector and the propagation length of the propagating SPs. Considering the complex geometry of the Ag NW, it is instructive to refer to the situation of SPs traveling at the interface between planar silver and glycerol. At visible spectral range, the absolute value of the real part of the permittivity of silver ε'_m is much larger than the imaginary part ε''_m. The permittivity of glycerol ε_d is also much smaller compared to $|\varepsilon'_m|$. Thus, the derivative versus temperature of the wave vector k_{sp} and the damping constant β (the inverse of propagation length) of the SP mode can be approximated as (Section 4 of Supporting Information):

$$\frac{\partial k_{sp}}{\partial T} \approx \frac{k_{sp}}{2(\varepsilon'_m + \varepsilon_d)} \cdot \left(\frac{\varepsilon'_m}{\varepsilon_d} \cdot \frac{\partial \varepsilon_d}{\partial T} + \frac{\varepsilon_d}{\varepsilon'_m} \cdot \frac{\partial \varepsilon'_m}{\partial T} \right) \quad (1)$$

$$\frac{\partial \beta}{\partial T} \approx \beta \cdot \left(\frac{3}{2\varepsilon_d} \cdot \frac{\partial \varepsilon_d}{\partial T} - \frac{2}{\varepsilon'_m} \cdot \frac{\partial \varepsilon'_m}{\partial T} + \frac{1}{\varepsilon''_m} \cdot \frac{\partial \varepsilon''_m}{\partial T} \right) \quad (2)$$

Clearly, the derivative of the wave vector and damping constant is determined by the combined actions of silver and

DOI: 10.1021/acsphotonics.9b00711
ACS Photonics 2019, 6, 2133–2140

the surrounding glycerol. With the rise of local temperature, the decreased permittivity of glycerol (ε_d) and silver (ε'_m) results in the decrease of the SP wave vector, corresponding to the reduced field confinement. After taking the TO parameters of glycerol and silver at room temperature and at the free space wavelength of 785 nm into eqs 1 and 2, we found that $\partial k_{sp}/\partial T$ is $-2.13e^{-4}k_{sp}$ and the contribution of glycerol to the derivative is more than 10× higher than that of silver. Because the increase of the damping constant due to the increased electron scattering in silver (the third term of eq 2) with the rise of temperature is higher than the decrease of the damping constant caused by the reduced field confinement (the first and second terms of eq 2), it results in the positive derivative of damping constant $\partial\beta/\partial T \approx 4.03e^{-3}\beta$.

For a Ag NW with finite length L surrounded by glycerol, the transmissivity, that is, the intensity of transmitted SPs at the output end of the NW I_{output} normalized to the original intensity of the SPs generated at the input NW end I_{input} can be expressed as (Section 5 of Supporting Information):

$$\eta = \frac{I_{output}}{I_{input}} \approx \frac{1-R}{e^{\beta L} - 2R + 4R\cdot\sin^2(2\pi n_{eff}L/\lambda + \phi)} \quad (3)$$

where $n_{eff} = k_{sp}/k_0$ is the effective refractive index of the SP mode, $k_0 = 2\pi/\lambda$ is the wave vector in free space, λ is wavelength, R is the reflectivity of SPs at the NW end, and ϕ is the intrinsic phase shift brought by the reflection at the NW ends. With the rise of environment temperature, the effective refractive index and the damping constant of the SPs on the Ag NW are decreased and increased, respectively. According to eq 3, the decreased effective refractive index results in the blue shift of the transmission spectrum for the Ag NW with length L. The enhanced damping constant always decreases the transmissivity of SPs. The blue shift and decreased intensity of the transmission spectrum induced by the temperature rise is consistent with the numerical simulation result in Figure 3a. The modulation depth of the transmissivity for each Celsius degree rise in temperature can be written as:

$$\Gamma = \frac{1}{\eta}\cdot\frac{\partial\eta}{\partial T} = -\frac{L\cdot\eta}{1-R}\cdot e^{\beta L}\cdot\frac{\partial\beta}{\partial T} - \Delta\cdot\frac{\lambda}{\eta\cdot k_{sp}}\cdot\frac{\partial k_{sp}}{\partial T} \quad (4)$$

where

$$\Delta = \frac{\partial\eta}{\partial\lambda} = \frac{4L\cdot R\cdot\eta^2\cdot k_{sp}}{(1-R)\cdot\lambda}\cdot\sin(4\pi n_{eff}L/\lambda + 2\phi) \quad (5)$$

is the slope value of the transmission spectrum at wavelength λ. Figure 4a,b show the effect of NW length on the transmissivity η, the slope value Δ, and the modulation depth Γ of propagating SPs on the NW. The propagation length of 7.3 μm and reflectivity of 0.23 for probe beam wavelength of 785 nm were experimentally obtained from the transmission spectra of Ag NWs with different lengths (Section 6 of Supporting Information). Based on the simulated electric field distribution of the NW upon probe beam excitation (Section 7 of Supporting Information), the wavelength of the SPs is obtained to be 430 nm. Therefore, the wave vector of the SPs is $2\pi/430$ nm^{-1}. The transmissivity possesses sinusoidal oscillations as the NW length increases (Figure 4a), and the maxima and minima correspond to the constructive and destructive interference between forward and backward propagating SPs, respectively. The reduction of the oscillation amplitude is caused by the increased ohmic loss for longer

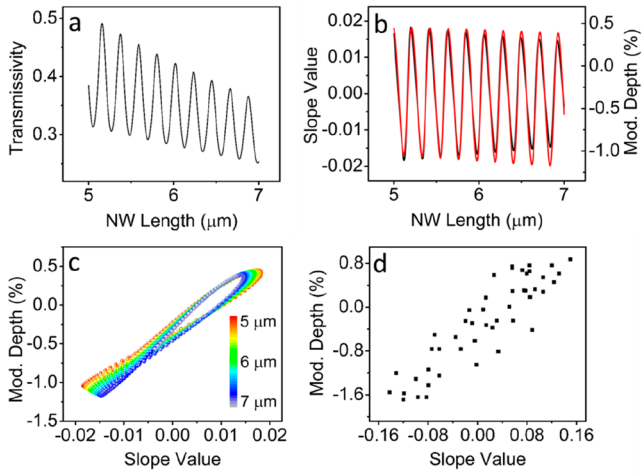

Figure 4. (a, b) Transmissivity (a), slope value (black line, b), and modulation depth (red line, b) of the propagating SPs as a function of NW length. (c, d) Theoretically analyzed (c) and experimentally measured (d) modulation depth as a function of the slope value of the transmission spectra at 785 nm wavelength. The colors of dots in (c) represent the length of NW.

NW. Both the slope value and the modulation depth of the transmissivity are periodically oscillated with the increment of the NW length (Figure 4b). According to eq 4, the modulation depth is approximately linearly proportional to the slope value of the transmission spectrum, which is confirmed in Figure 4c. Since the first term of eq 4 is negative, the maximum absolute value of the negative modulation depth (1.18%) is larger than the maximum positive modulation depth (0.46%). In experiment, we measured the photothermal modulation depth of 46 NWs under the control beam excitation at the middle section of the NW with the polarization perpendicular to the NW. The length of the NW was mostly distributed in the range of 5−7 μm. Figure 4d shows the obtained photothermal modulation depth as a function of the corresponding slope value of the measured transmission spectrum at wavelength of 785 nm. In accordance with the theoretical result, the experimentally measured modulation depth approximately linearly increases with the increment of the slope value, and the maximum absolute values of the positive and negative modulation depth are different. The significant difference in slope value between theoretical and experimental results (Figure 4c,d) is caused by the existence of a scaling factor between the transmissivity defined in the theoretical analysis and the experiment.

We also explored the influence of the control beam power on the modulation of the propagating SPs on Ag NW. Figure 5a displays the variation of the modulation depth as a function of the control beam power for the two NWs studied in Figure 2. Clearly, with the increase of the control beam power, the intensity of transmitted SPs of the NW I was first increased, reaching the maximum at an incident power of about 30 mW, corresponding to a modulation depth of 15%, and then started decreasing. The power dependence of the NW II is opposite to the NW I, and the minimum value of the modulation depth is −25%. The first increase or decrease of the transmitted SP intensity is caused by the blue shift of the transmission spectrum, which is consistent with the experimental result in Figure 2j and the simulation result in Figure 3a. The intensity of transmitted SPs reaches the maximum (minimum) when one of the FP resonance peak (valley) is at the wavelength of

DOI: 10.1021/acsphotonics.9b00711
ACS Photonics 2019, 6, 2133−2140

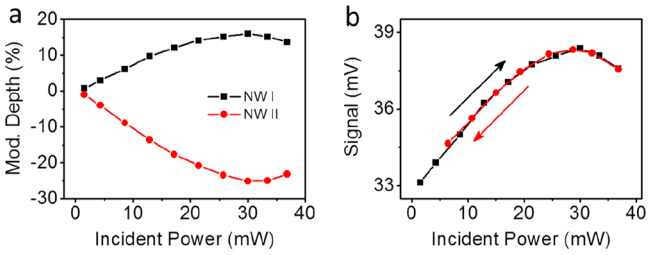

Figure 5. (a) Variation of the modulation depth as a function of the control beam power for the NW I and NW II shown in Figure 2. (b) Variation of the transmitted SP signal as a function of the control beam power for the NW I. The black and red dot lines correspond to the process of increasing and decreasing the incident power, respectively. The control laser beam was focused at the middle of the NW with polarization perpendicular to the NW axis.

the probe beam. The further blue shift of the transmission spectrum results in the decrease and increase of the transmitted SP intensity for the NW I and II, respectively. The power dependence of the photothermal modulation of the transmitted SPs is reversible. Figure 5b shows the measured voltage signal of the transmitted SPs for the sequence of increasing and decreasing the control beam power for the NW I. As can be seen, the voltage signal for the process of decreasing the control beam power reproduces the result of the increasing power process. This reversible photothermal modulation also indicates the control laser did not cause damage to the Ag NW.

In order to determine the temporal response of the photothermal modulation of propagating SPs on Ag NW, we studied the intensity variation of the transmitted SPs when the control beam was repeatedly switched on and off. In the dynamic measurements, the signal of transmitted SPs from the NW output end was monitored in real time with an oscilloscope. The control beam was modulated with a period of 50 μs and a duty cycle of 50%. Figure 6a illustrates the

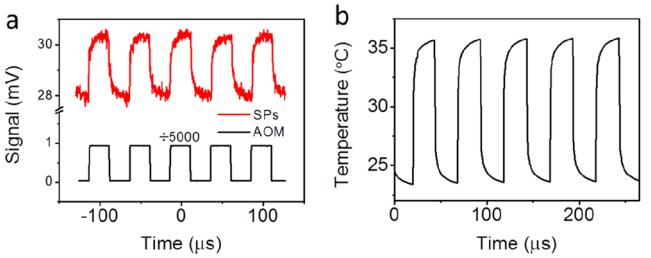

Figure 6. (a) Measured temporal response of the transmitted SPs at the NW end (red line). The AOM is driven by a square-wave reference signal (5 V) with duty cycle of 50% and period of 50 μs (black line). The amplitude of the square wave in the plot is divided by 5000. (b) Simulated variation of temperature at the position 20 nm away from the NW surface under control beam illumination. The control beam with power of 20 mW and polarization perpendicular to the NW axis is modulated by a square-wave (duty cycle of 50% and period of 50 μs) and incident on the middle of the NW.

temporal response of transmitted SPs to the control beam excitation on a Ag NW whose modulation depth is positive. The control beam is focused at the middle section of the NW with power of about 20 mW and polarization perpendicular to the NW axis. Abrupt increase and decrease in the transmitted SP signal was observed when the control beam was turned on and off, respectively. The measured signal rise time from 10% to 90% of the maximum voltage is 4.6 μs and the fall time is 6.5 μs. We also studied the change of photothermal modulation depth as a function of period of the modulation for the Ag NW shown in Figure 2a–e (see Section 8 of Supporting Information). The result shows that the modulation depth starts to dramatically reduce when the period is smaller than 20 μs, which is consistent with the measured response time. Transient thermal response of the Ag NW-glycerol system upon control beam excitation was numerically simulated, where the temporal function of the ohmic loss generated by the control beam is a square wave with time period of 50 μs and duty cycle of 50%. The variation of the temperature in glycerol during on–off switching operation of the heat source is presented in Figure 6b. The simulated rise and fall time is 4.5 and 5.2 μs, respectively, which is consistent with our experimental result.

CONCLUSION

In conclusion, we systematically studied the influence of photothermal effect on the propagation properties of SPs on an extremely compact Ag NW plasmonic waveguide. Because of the TO effect, the rise of local temperature, induced by the heat generation of Ag NW under the excitation of control beam of 532 nm wavelength, results in the reduction of wave vector and propagation length of the propagating SPs generated by a probe beam of 785 nm wavelength. The intensity of the transmitted SPs at the NW end is increased or decreased dramatically, depending on the slope value of the transmission spectrum at the probe beam wavelength. The amplitude of the photothermal modulation depth is strongly dependent on the focal position, polarization, and power of the control beam. The simulations reveal that the high modulation depth at the NW end is mainly caused by the heat generation induced by the propagating SPs on the NW. The analytical solutions for the transmissivity and modulation depth are provided, which well explain our experimental results. The measurement of the dynamic photothermal modulation process shows a response time of about 5 μs. Our work not only demonstrates a new all-optical modulation method for the propagating SPs on plasmonic nanowire waveguides, but also provides the basic understanding about the influence of environment temperature on the propagating SPs.

METHODS

Sample Preparation. The sample cell for experiment consists of two piranha solution cleaned glass coverslips separated by a rubber O-ring with a thickness of about 3 mm. The Ag NWs prepared using a solution-phase polyol method[50] were first spin-coated on top of the bottom coverslip with marked grids, which can help to find the same structure with both optical microscope and SEM. Then a rubber O-ring was put on the bottom slide, and 100 μL of glycerol was dropped inside the ring. Finally, the cell was assembled by putting another glass coverslip on top of the rubber O-ring.

Experimental Setup. The experimental setup is based on a home-built confocal microscope using two laser sources (Figure 1). A solid-state laser at 532 nm wavelength provided the optical control beam. The laser beam intensity was modulated using an AOM (CNI). After spatially filtered, the control beam was focused onto the sample using a 100× oil immersion objective (NA 1.4, Olympus). Its focal spot on the sample plane was steered using a galvanometer scanning mirror

DOI: 10.1021/acsphotonics.9b00711
ACS Photonics 2019, 6, 2133–2140

(GVS012, Thorlabs) and a telescopic system with a step size of 40 nm. The probe laser beam from a 785 nm laser diode was focused on the Ag NW end to excite the propagating SPs on the NW. The transmitted SPs at the other end of the NW was separated from the scattered control laser light by an interference filter and directed to an avalanche photodiode (APD410A, Thorlabs) through a spatial filter system which collected the light from an area of about 1.0 μm in diameter on the sample surface. The intensity variation of the transmitted SPs δP induced by the control laser beam was obtained using a lock-in amplifier (SR830, SRS) that was referenced to the repetition rate of the AOM. The intensity of the transmitted SPs P in absence of the control beam was recorded with a digital voltmeter (2182A, Keithley). The signal from the lock-in amplifier and the digital voltmeter were recorded by a data acquisition card (PXIe-6341, National Instruments). Analysis and presentation of the recorded data were performed via an algorithm written in LabVIEW (LabVIEW 2014, National Instruments). In the dynamic experiments, the voltage signal of the transmitted SPs was recorded with an oscilloscope (DSO5054A, Agilent). The beam waist of the control and probe Gaussian beams are 0.63 and 0.8 μm, respectively. The power of the probe beam is about 10 μW, which is more than 100× lower than that of the control beam. Therefore, the rise of local temperature induced by the probe beam is negligible. The used power and modulation frequency of the control beam for studying the focal position and polarization dependence are 1.3 mW (corresponding to power density of 0.42 MW/cm^2) and 80 kHz, respectively. The used modulation frequency is 25 kHz when we studied the influence of the control beam power on the modulation of the propagating SPs.

Numerical Simulations. The three-step simulations were performed by combining the "Wave Optics-Frequency Domain" module and "Heat Transfer" module in a finite element method based commercial software (COMSOL Multiphysics). The geometry was modeled as a cylinder Ag NW lying on a glass substrate with glycerol on top. The diameter and the length of the NW is 120 nm and 6.29 μm, respectively. The beam waist of the control and probe Gaussian beam are both 0.8 μm. The incident power of the probe Gaussian beam is 10 μW. The first step in the simulation was to calculate the ohmic loss caused by the control laser, which is a full wave electromagnetic simulation. A port boundary condition was used to define the control Gaussian beam and the corresponding incident power. In the second step, the ohmic loss generated above was used as the heat source to simulate the heating process. Here we consider the heating process as a time-dependent problem. The temperature response time of the system is about a few microseconds, so we set the heating time to 50 μs to ensure that the system is close to equilibrium. We used the infinite-domain boundary condition to simulate the infinite outer space. The initial and the ambient temperature was set to 23 °C. In the last step, a probe Gaussian beam was applied at one of the NW ends to excite propagating SPs. The transmission spectrum of the propagating SPs was calculated by integrating the transmitted power flow over a range of 60° solid angle at the output end of the NW.

■ ASSOCIATED CONTENT

Supporting Information

The Supporting Information is available free of charge on the ACS Publications website at DOI: 10.1021/acsphotonics.9b00711.

The thermal and optical constants for selected materials, dispersion relation of the propagating SPs on Ag NW under different environment temperature, mode analysis of the propagating SPs on Ag NW, the derivative of wave vector and damping constant with respect to temperature, the transmissivity of propagating SPs at the Ag NW end, the NW end reflectivity and the propagation length of SPs, the electric field distribution of the NW upon probe beam excitation, the photothermal modulation depth as a function of the modulation period (PDF)

■ AUTHOR INFORMATION

Corresponding Author

*E-mail: weihong@iphy.ac.cn.

ORCID

Li Chen: 0000-0002-0582-1903

Hongxing Xu: 0000-0002-1718-8834

Hong Wei: 0000-0002-3616-0386

Author Contributions

‖Q.L. and L.C. contributed equally to this work.

Notes

The authors declare no competing financial interest.

■ ACKNOWLEDGMENTS

This work was supported by The Ministry of Science and Technology of China (Grant 2015CB932400), National Natural Science Foundation of China (Grants 11422436, 11774413, 11674256, 11704133, and 91850207), the "Strategic Priority Research Program (B)" (Grant XDB07030100) of Chinese Academy of Sciences, and the Foundation for Distinguished Young Talents in Higher Education of Guangdong (Grant 2016KQNCX031).

■ REFERENCES

(1) Ozbay, E. Plasmonics: Merging Photonics and Electronics at Nanoscale Dimensions. *Science* **2006**, *311*, 189−193.

(2) Sorger, V. J.; Oulton, R. F.; Ma, R. M.; Zhang, X. Toward Integrated Plasmonic Circuits. *MRS Bull.* **2012**, *37*, 728−738.

(3) Wei, H.; Xu, H. X. Nanowire-Based Plasmonic Waveguides and Devices for Integrated Nanophotonic Circuits. *Nanophotonics* **2012**, *1*, 155−169.

(4) Xiong, X.; Zou, C. L.; Ren, X. F.; Liu, A. P.; Ye, Y. X.; Sun, F. W.; Guo, G. C. Silver Nanowires for Photonics Applications. *Laser Photonics Rev.* **2013**, *7*, 901−919.

(5) Wei, H.; Pan, D.; Zhang, S. P.; Li, Z. P.; Li, Q.; Liu, N.; Wang, W. H.; Xu, H. X. Plasmon Waveguiding in Nanowires. *Chem. Rev.* **2018**, *118*, 2882−2926.

(6) Guo, X.; Ma, Y. G.; Wang, Y. P.; Tong, L. M. Nanowire Plasmonic Waveguides, Circuits and Devices. *Laser Photonics Rev.* **2013**, *7*, 855−881.

(7) Weeber, J. C.; Krenn, J. R.; Dereux, A.; Lamprecht, B.; Lacroute, Y.; Goudonnet, J. P. Near-Field Observation of Surface Plasmon Polariton Propagation on Thin Metal Stripes. *Phys. Rev. B: Condens. Matter Mater. Phys.* **2001**, *64*, 045411.

(8) Bozhevolnyi, S. I.; Volkov, V. S.; Devaux, E.; Laluet, J. Y.; Ebbesen, T. W. Channel Plasmon Subwavelength Waveguide

DOI: 10.1021/acsphotonics.9b00711
ACS Photonics 2019, 6, 2133−2140

Components Including Interferometers and Ring Resonators. *Nature* **2006**, *440*, 508−511.
(9) Cai, W. S.; Shin, W.; Fan, S. H.; Brongersma, M. L. Elements for Plasmonic Nanocircuits with Three-Dimensional Slot Waveguides. *Adv. Mater.* **2010**, *22*, 5120−5123.
(10) Sanders, A. W.; Routenberg, D. A.; Wiley, B. J.; Xia, Y. N.; Dufresne, E. R.; Reed, M. A. Observation of Plasmon Propagation, Redirection, and Fan-out in Silver Nanowires. *Nano Lett.* **2006**, *6*, 1822−1826.
(11) Ditlbacher, H.; Hohenau, A.; Wagner, D.; Kreibig, U.; Rogers, M.; Hofer, F.; Aussenegg, F. R.; Krenn, J. R. Silver Nanowires as Surface Plasmon Resonators. *Phys. Rev. Lett.* **2005**, *95*, 257403.
(12) Zhang, S. P.; Wei, H.; Bao, K.; Hakanson, U.; Halas, N. J.; Nordlander, P.; Xu, H. X. Chiral Surface Plasmon Polaritons on Metallic Nanowires. *Phys. Rev. Lett.* **2011**, *107*, 096801.
(13) Wei, H.; Tian, X. R.; Pan, D.; Chen, L.; Jia, Z. L.; Xu, H. X. Directionally-Controlled Periodic Collimated Beams of Surface Plasmon Polaritons on Metal Film in Ag Nanowire/Al_2O_3/Ag Film Composite Structure. *Nano Lett.* **2015**, *15*, 560−564.
(14) Li, Q.; Pan, D.; Wei, H.; Xu, H. X. Plasmon-Assisted Selective and Super-Resolving Excitation of Individual Quantum Emitters on a Metal Nanowire. *Nano Lett.* **2018**, *18*, 2009−2015.
(15) Li, Z. P.; Bao, K.; Fang, Y. R.; Huang, Y. Z.; Nordlander, P.; Xu, H. X. Correlation between Incident and Emission Polarization in Nanowire Surface Plasmon Waveguides. *Nano Lett.* **2010**, *10*, 1831−1835.
(16) Li, Z. P.; Hao, F.; Huang, Y. Z.; Fang, Y. R.; Nordlander, P.; Xu, H. X. Directional Light Emission from Propagating Surface Plasmons of Silver Nanowires. *Nano Lett.* **2009**, *9*, 4383−4386.
(17) Akimov, A. V.; Mukherjee, A.; Yu, C. L.; Chang, D. E.; Zibrov, A. S.; Hemmer, P. R.; Park, H.; Lukin, M. D. Generation of Single Optical Plasmons in Metallic Nanowires Coupled to Quantum Dots. *Nature* **2007**, *450*, 402−406.
(18) Fedutik, Y.; Temnov, V. V.; Schops, O.; Woggon, U.; Artemyev, M. V. Exciton-Plasmon-Photon Conversion in Plasmonic Nanostructures. *Phys. Rev. Lett.* **2007**, *99*, 136802.
(19) Wei, H.; Ratchford, D.; Li, X. Q.; Xu, H. X.; Shih, C. K. Propagating Surface Plasmon Induced Photon Emission from Quantum Dots. *Nano Lett.* **2009**, *9*, 4168−4171.
(20) Fang, Y. R.; Li, Z. P.; Huang, Y. Z.; Zhang, S. P.; Nordlander, P.; Halas, N. J.; Xu, H. X. Branched Silver Nanowires as Controllable Plasmon Routers. *Nano Lett.* **2010**, *10*, 1950−1954.
(21) Wei, H.; Zhang, S. P.; Tian, X. R.; Xu, H. X. Highly Tunable Propagating Surface Plasmons on Supported Silver Nanowires. *Proc. Natl. Acad. Sci. U. S. A.* **2013**, *110*, 4494−4499.
(22) Wei, H.; Pan, D.; Xu, H. X. Routing of Surface Plasmons in Silver Nanowire Networks Controlled by Polarization and Coating. *Nanoscale* **2015**, *7*, 19053−19059.
(23) Wei, H.; Wang, Z. X.; Tian, X. R.; Kall, M.; Xu, H. X. Cascaded Logic Gates in Nanophotonic Plasmon Networks. *Nat. Commun.* **2011**, *2*, 387.
(24) Wei, H.; Li, Z. P.; Tian, X. R.; Wang, Z. X.; Cong, F. Z.; Liu, N.; Zhang, S. P.; Nordlander, P.; Halas, N. J.; Xu, H. X. Quantum Dot-Based Local Field Imaging Reveals Plasmon-Based Interferometric Logic in Silver Nanowire Networks. *Nano Lett.* **2011**, *11*, 471−475.
(25) Maier, S. A. *Plasmonics: Fundamentals and Applications*; Springer: New York, 2007.
(26) Nikolajsen, T.; Leosson, K.; Bozhevolnyi, S. I. Surface Plasmon Polariton Based Modulators and Switches Operating at Telecom Wavelengths. *Appl. Phys. Lett.* **2004**, *85*, 5833−5835.
(27) Lereu, A. L.; Passian, A.; Goudonnet, J. P.; Thundat, T.; Ferrell, T. L. Optical Modulation Processes in Thin Films Based on Thermal Effects of Surface Plasmons. *Appl. Phys. Lett.* **2005**, *86*, 154101.
(28) Gosciniak, J.; Bozhevolnyi, S. I. Performance of Thermo-Optic Components Based on Dielectric-Loaded Surface Plasmon Polariton Waveguides. *Sci. Rep.* **2013**, *3*, 1803.
(29) Schildkraut, J. S. Long-Range Surface Plasmon Electrooptic Modulator. *Appl. Opt.* **1988**, *27*, 4587−4590.
(30) Dionne, J. A.; Diest, K.; Sweatlock, L. A.; Atwater, H. A. PlasMOStor: A Metal−Oxide−Si Field Effect Plasmonic Modulator. *Nano Lett.* **2009**, *9*, 897−902.
(31) Babicheva, V. E.; Boltasseva, A.; Lavrinenko, A. V. Transparent Conducting Oxides for Electro-Optical Plasmonic Modulators. *Nanophotonics* **2015**, *4*, 165−185.
(32) MacDonald, K. F.; Sámson, Z. L.; Stockman, M. I.; Zheludev, N. I. Ultrafast Active Plasmonics. *Nat. Photonics* **2009**, *3*, 55−58.
(33) Abb, M.; Albella, P.; Aizpurua, J.; Muskens, O. L. All-Optical Control of A Single Plasmonic Nanoantenna-ITO Hybrid. *Nano Lett.* **2011**, *11*, 2457−2463.
(34) Rude, M.; Simpson, R. E.; Quidant, R.; Pruneri, V.; Renger, J. Active Control of Surface Plasmon Waveguides with a Phase Change Material. *ACS Photonics* **2015**, *2*, 669−674.
(35) Pala, R. A.; Shimizu, K. T.; Melosh, N. A.; Brongersma, M. L. A Nonvolatile Plasmonic Switch Employing Photochromic Molecules. *Nano Lett.* **2008**, *8*, 1506−1510.
(36) Chen, J. J.; Li, Z.; Yue, S.; Gong, Q. H. Highly Efficient All-Optical Control of Surface-Plasmon-Polariton Generation Based on a Compact Asymmetric Single Slit. *Nano Lett.* **2011**, *11*, 2933−2939.
(37) Krasavin, A. V.; Vo, T. P.; Dickson, W.; Bolger, P. M.; Zayats, A. V. All-Plasmonic Modulation via Stimulated Emission of Copropagating Surface Plasmon Polaritons on A Substrate with Gain. *Nano Lett.* **2011**, *11*, 2231−2235.
(38) Weeber, J. C.; Hassan, K.; Saviot, L.; Dereux, A.; Boissière, C.; Durupthy, O.; Chaneac, C.; Burov, E.; Pastouret, A. Efficient Photo-Thermal Activation of Gold Nanoparticle-Doped Polymer Plasmonic Switches. *Opt. Express* **2012**, *20*, 27636.
(39) Okamoto, T.; Kamiyama, T.; Yamaguchi, I. All-Optical Spatial Light Modulator with Surface Plasmon Resonance. *Opt. Lett.* **1993**, *18*, 1570−1572.
(40) Kaya, S.; Weeber, J. C.; Zacharatos, F.; Hassan, K.; Bernardin, T.; Cluzel, B.; Fatome, J.; Finot, C. Photo-Thermal Modulation of Surface Plasmon Polariton Propagation at Telecommunication Wavelengths. *Opt. Express* **2013**, *21*, 22269−22284.
(41) Weeber, J. C.; Bernardin, T.; Nielsen, M. G.; Hassan, K.; Kaya, S.; Fatome, J.; Finot, C.; Dereux, A.; Pleros, N. Nanosecond Thermo-Optical Dynamics of Polymer Loaded Plasmonic Waveguides. *Opt. Express* **2013**, *21*, 27291−27305.
(42) Huang, X. H.; El-Sayed, M. A. Gold Nanoparticles: Optical Properties and Implementations in Cancer Diagnosis and Photothermal Therapy. *J. Adv. Res.* **2010**, *1*, 13−28.
(43) Lal, S.; Clare, S. E.; Halas, N. J. Nanoshell-Enabled Photothermal Cancer Therapy: Impending Clinical Impact. *Acc. Chem. Res.* **2008**, *41*, 1842−1851.
(44) Alkilany, A. M.; Thompson, L. B.; Boulos, S. P.; Sisco, P. N.; Murphy, C. J. Gold Nanorods: Their Potential for Photothermal Therapeutics and Drug Delivery, Tempered by the Complexity of Their Biological Interactions. *Adv. Drug Delivery Rev.* **2012**, *64*, 190−199.
(45) Ou, Y.-C.; Webb, J. A.; Faley, S.; Shae, D.; Talbert, E. M.; Lin, S.; Cutright, C. C.; Wilson, J. T.; Bellan, L. M.; Bardhan, R. Gold Nanoantenna-Mediated Photothermal Drug Delivery from Thermosensitive Liposomes in Breast Cancer. *ACS Omega* **2016**, *1*, 234−243.
(46) Gaiduk, A.; Yorulmaz, M.; Ruijgrok, P. V.; Orrit, M. Room-Temperature Detection of A Single Molecule's Absorption by Photothermal Contrast. *Science* **2010**, *330*, 353−356.
(47) Gaiduk, A.; Ruijgrok, P. V.; Yorulmaz, M.; Orrit, M. Detection Limits in Photothermal Microscopy. *Chem. Sci.* **2010**, *1*, 343−350.
(48) Selmke, M.; Braun, M.; Cichos, F. Photothermal Single-Particle Microscopy: Detection of a Nanolens. *ACS Nano* **2012**, *6*, 2741−2749.
(49) Yorulmaz, M.; Nizzero, S.; Hoggard, A.; Wang, L.-Y.; Cai, Y.-Y.; Su, M.-N.; Chang, W.-S.; Link, S. Single-Particle Absorption Spectroscopy by Photothermal Contrast. *Nano Lett.* **2015**, *15*, 3041−3047.
(50) Sun, Y. G.; Xia, Y. N. Large-Scale Synthesis of Uniform Silver Nanowires Through a Soft, Self-Seeding, Polyol Process. *Adv. Mater.* **2002**, *14*, 833−837.

DOI: 10.1021/acsphotonics.9b00711
ACS Photonics 2019, 6, 2133−2140